

Numerical Simulations of IBC Solar Cells Based on Poly-Si Carrier-Selective Passivating Contacts

Procel, Paul; Yang, Guangtao; Isabella, Olindo; Zeman, Miro

DOI

[10.1109/JPHOTOV.2019.2892527](https://doi.org/10.1109/JPHOTOV.2019.2892527)

Publication date

2019

Document Version

Final published version

Published in

IEEE Journal of Photovoltaics

Citation (APA)

Procel, P., Yang, G., Isabella, O., & Zeman, M. (2019). Numerical Simulations of IBC Solar Cells Based on Poly-Si Carrier-Selective Passivating Contacts. *IEEE Journal of Photovoltaics*, 9(2), 374-384. Article 8626188. <https://doi.org/10.1109/JPHOTOV.2019.2892527>

Important note

To cite this publication, please use the final published version (if applicable). Please check the document version above.

Copyright

Other than for strictly personal use, it is not permitted to download, forward or distribute the text or part of it, without the consent of the author(s) and/or copyright holder(s), unless the work is under an open content license such as Creative Commons.

Takedown policy

Please contact us and provide details if you believe this document breaches copyrights. We will remove access to the work immediately and investigate your claim.

Green Open Access added to TU Delft Institutional Repository

'You share, we take care!' – Taverne project

<https://www.openaccess.nl/en/you-share-we-take-care>

Otherwise as indicated in the copyright section: the publisher is the copyright holder of this work and the author uses the Dutch legislation to make this work public.

Numerical Simulations of IBC Solar Cells Based on Poly-Si Carrier-Selective Passivating Contacts

Paul Procel , Guangtao Yang, Olindo Isabella , and Miro Zeman

Abstract—This paper presents an analysis of physical mechanisms related to operation and optimization of interdigitated back contact (IBC) poly-silicon-based devices. Concepts of carrier selectivity and tunneling are used to identify the parameters that impact on the fill factor. Then, based on technology computer-aided design (TCAD) numerical simulations, we describe the device performance in terms of transport and passivation. A validation of the model is performed by matching measured and simulated R, T, and external quantum efficiency spectra and electrical parameters. As result of such process, the opto-electrical losses of the reference device are identified. Then, we execute a study of the impact of process parameters on the performance of the IBC device under analysis. Assuming a uniform SiO₂ layer, simulation results reveal that both n-type and p-type poly-Si contacts can be theoretically *perfect* (i.e., approx. lossless), if assuming no interface recombination but considering tunneling of both carrier types. In other words, there exists an optimum oxide thickness (1 nm) for which majority carriers tunneling works already very well, and minority tunneling is still low enough to not result in significant recombination. Moreover, SiO₂ thickness up to maximum 1.6 nm is crucial to achieve high efficiency. Regarding rear geometry analysis, the efficiency curve as a function of emitter width peaks at 70% of pitch coverage. Further, it is shown that diffused dopants inside crystalline silicon make the device resilient to passivation quality. Finally, the calibrated model is used to perform an optimization study aiming at calculating the performance limit. The estimated performance limit is 27.3% for a 100- μ m-thick bulk, 20-nm-thick poly-silicon layers, silver as rear contact, and double ARC.

Index Terms—IBC solar cells, passivating contacts, poly-silicon, semiconductors device modeling.

I. INTRODUCTION

CRYSTALLINE silicon (c-Si) solar cells are leading the actual photovoltaic (PV) market due to abundance of raw material, stability, technological development, conversion efficiency, and cost effectiveness [1]. Simultaneously, the PV market aims at reducing costs of generated electrical power by increasing solar cells efficiency and minimizing production cost. To achieve this objective, research and development groups devoted several works on novel concepts to reduce device recombination losses and on advanced solar cell architectures [2].

Manuscript received December 19, 2018; accepted December 28, 2018. Date of publication January 25, 2019; date of current version February 18, 2019. This work was supported by the European Union's Horizon2020 Programme for Research, Technological Development and Demonstration in the framework of NextBase Project under Grant 727523. (Corresponding author: Paul Procel.)

The authors are with the Delft University of Technology, 2628 CD Delft, The Netherlands (e-mail: P.A.procelmoya@tudelft.nl; G.Yang@tudelft.nl; O.isabella@tudelft.nl; M.Zeman@tudelft.nl).

Color versions of one or more of the figures in this paper are available online at <http://ieeexplore.ieee.org>.

Digital Object Identifier 10.1109/JPHOTOV.2019.2892527

Concerning solar cell architectures, interdigitated back contact (IBC) concept stands as the main option to demonstrate remarkable efficiencies [3]–[8] owing to the absence of front shading contact. To increase the conversion efficiency of solar cells, it is crucial to reduce the recombination losses that are typically related to highly defective metal/semiconductor interfaces in conventional homo-junction devices. One approach to quench such recombination losses consists in reducing metal/c-Si interface using point contacts. However, this approach demands additional lithography steps with still limited open-circuit voltage V_{oc} [9]–[11] (below 700 mV). On the other hand, passivating carrier-selective contacts (CSCs) effectively reduce such recombination losses, demonstrating high V_{oc} well above 715 mV for high- [12]–[14] and low-temperature processes [6], [8], [15]–[17]. High-thermal budget CSCs commonly deploy a thin SiO₂ passivating layer beneath highly doped poly-silicon (alloys). This approach is of particular interest owing to its compatibility with industrial thermal budgets. Moreover, recent results report outstanding V_{oc} values well above 700 mV [14], [18]–[25], anticipating conversion efficiency above 26% [3] when combining CSCs with IBC solar cell architecture.

Like silicon heterojunction (SHJ) contacts based on hydrogenated amorphous silicon, the core of such high-efficiency devices stands on transport mechanisms. Several studies have been reported to explain the inner physics of poly-silicon (poly-Si) based CSCs. Accordingly, two different approaches have been proposed to describe transport through the thin oxide layer: carrier transport via pinhole in oxide layer [26], [27], and tunneling of carriers through ultra-thin oxide layers [28], [29]. In the first case, pinholes are formed by increasing the annealing temperature above 1000 °C in oxide layers above 2 nm [20]. In the second case, the transport of carriers is described by tunneling through a potential energy barrier built by an oxide layer around 1.5 nm thick [22], [30]–[33], implying process temperatures lower than 950 °C. It is worth noting that several studies within state-of-the-art complementary metal oxide semiconductor (CMOS) devices [34]–[40] confirm that leakage currents through thin dielectrics are based on tunneling. In such a context, theoretical works describing transport mechanisms have been carried out to explain the potential of CSCs based on oxide as passivating layer [28], [41] for front and rear contact structures.

Here, based on an advanced two-dimensional opto-electrical model, we investigate the mechanisms leading to main losses in poly-Si-based IBC reference solar cell [22]. After, we identify the main competitive physical mechanisms that are related to process fabrication and enable high fill factor (FF) and V_{oc} .

Finally, we present the ultimate potential of poly-Si-based CSCs combined with IBC architecture.

It is worth noting that our simulation platform assumes that CSC transport is exclusively based on direct tunneling through a uniform tunneling oxide layer [28], [41] neglecting pinhole-based transport contribution [26], [27], [42], [43]. Such a methodology has been successfully applied to advanced semiconductor devices design and processes [34]–[40], [44]–[46], from which material properties like tunneling masses and thermionic emission parameters are also taken [34]. In this paper, we do not perform an extensive experimental characterization to assess the applicability of contradicting transport mechanisms (tunneling or pinholes) for solar cell devices processes [47], [48]. Accordingly, the presented results and conclusions should be interpreted taking this in account.

II. CONTACT SELECTIVITY AND TRANSPORT

A. Contact Selectivity

Considering the definition of contact selectivity (S) proposed in [49] at the latest portion of c-Si, beneath the tunneling oxide interface, we have

$$S_n = \frac{n \cdot \mu_e}{p \cdot \mu_h}, \quad S_p = \frac{p \cdot \mu_h}{n \cdot \mu_e} \quad (1)$$

where n and p are electrons and holes concentration, and μ_e and μ_h are electron and hole mobility, respectively. As in c-Si μ_n and μ_p are in the same order of magnitude, the fundament of high selectivity stands on the asymmetric carrier concentrations at the interface [49]. Accordingly, the contact selectivity is maximized by increasing the carrier concentration of one type of carriers and dually decreasing the concentration of the other.

Since selectivity and transport of poly-Si-based CSC are symmetrical for collecting electrons or holes (see Fig. 1), we describe physical mechanisms related to electrons in the conduction band as reference. Such an assumption is here valid as poly-Si features a bandgap close to that of c-Si; then, similar phenomena are expected for holes in the valence band.

In general, carrier concentrations at c-Si/SiO₂ interface are so defined

$$n = \Delta n + N_D = N_C \cdot e^{-\left(\frac{E_{C,cSi} - E_{f_n,cSi}}{kT}\right)} = N_C \cdot e^{-\left(\frac{\Delta E_e}{kT}\right)} \quad (2)$$

where N_C is the density of states in the conduction band for electrons, $E_{f_n,cSi}$ stands for quasi-Fermi energy level of electrons at c-Si/SiO₂ interface, $E_{C,cSi}$ is the conduction band energy, N_D is the donor density, and Δn is the free carrier injection density. Thus, for n-type contact and at the c-Si/SiO₂ interface, n is maximized when $\Delta E_e = E_{C,cSi} - E_{f_n,cSi}$ is a negative number, meaning that $E_{C,cSi} < E_{f_n,cSi}$ while for p-type contact and at the c-Si/SiO₂ interface, p is maximized when $\Delta E_h = E_{f_h,cSi} - E_{V,cSi}$ is negative, in other words $E_{V,cSi} > E_{f_h,cSi}$. This can be attained by maximizing the band bending in c-Si leveraging on the built-in voltage V_{bi} [50]. In case of SHJ, to induce a strong c-Si band bending, the contact material fabrication process allows flexibility to set the proper Fermi energy for maximized V_{bi} at low temperature [50]. If

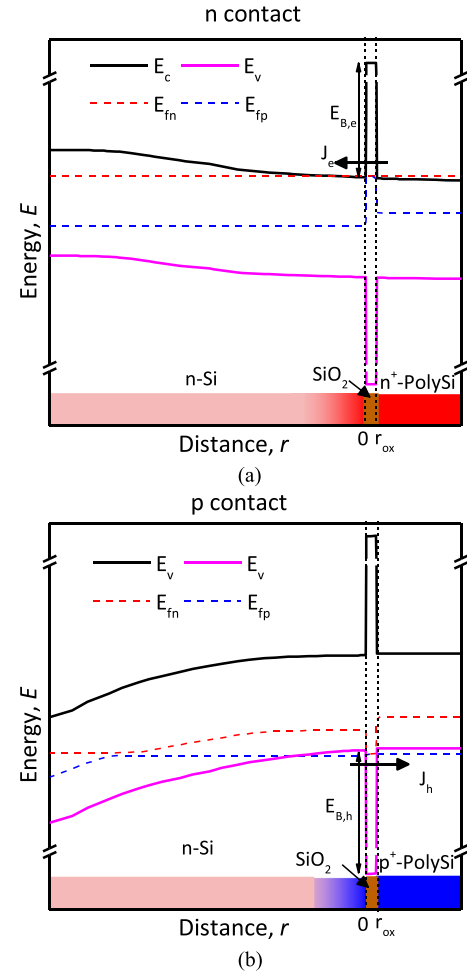


Fig. 1. Schematic band diagram of (a) n-type and (b) p-type contacts for a poly-Si-based solar cell under illumination. Distance $r = 0$ is set at c-Si/SiO₂ interface. $E_{C,cSi}$ ($E_{V,cSi}$) and E_{f_n} (E_{f_h}) are conduction (valence) band energy level and quasi-Fermi level of electrons (holes), respectively; $E_{B,e}$ and $E_{B,h}$ are the energy potential barriers built by SiO₂ for electron and holes, respectively.

contact material properties do not allow a strong band bending (i.e., poly-Si alloys), n and p can be also maximized with the support of active dopants diffused inside c-Si as a result of dopants activation temperature [51]. Importantly, according to (2), ΔE_e and ΔE_h are also minimized if doping peak concentration at c-Si/SiO₂ interface is higher than N_C ($3.2 \times 10^{19} \text{ cm}^{-3}$) for n-type contact and higher than N_V ($1.8 \times 10^{19} \text{ cm}^{-3}$) for p-type contact, thus maximizing contact selectivity.

B. Tunneling

In CSCs-IBC solar cells, the collection of carriers involves transport through two heterointerfaces. Poly-Si CSC interfaces consist of 1) c-Si passivated by a thin SiO₂ layer subsequently 2) covered by a highly doped poly-Si layer. Such structures exhibit peculiar discontinuities in the band diagram [see Fig. 1(a) and (b)]. Assuming a uniform (i.e., no pinholes) SiO₂ layer, carrier collection is described by tunneling transport mechanisms. These mechanisms describe the transport of carriers with enough

energy to cross through a potential energy barrier. The energy of carriers, the occupied and free states in both sides of the barrier, and the energy barrier are therefore crucial parameters. As described by Jeong *et al.* [45], the tunneling for transport of electrons and holes is, therefore, related to the local generation rate G as follows:

$$G_e = \frac{A \cdot T}{k} \cdot \xi \cdot \Gamma_e(r_{ox}) \cdot \ln \left(\frac{1 + \exp \left[-\frac{\Delta E_e}{kT} \right]}{1 + \exp \left[-\frac{E_{e,cSi} - E_{f_e,n}}{kT} \right]} \right) \quad (3)$$

where A stands for Richardson constant, T is temperature, k is the Boltzmann constant, ξ is the electrical field, $\Gamma_e(r_{ox})$ is the tunneling probability in SiO_2 layer, ΔE_e is the energy of collecting carriers at c-Si/ SiO_x interface with respect to Fermi energy ($E_{e,cSi} - E_{f_e,cSi}$) of electrons in the conduction band and E_{f_e} is the quasi-Fermi level of electrons at each side of energy barrier, either c-Si/ SiO_2 (c-Si) or doped poly-Si/ SiO_2 . The subscript n indicates n-type contact. The term inside the logarithm correlates the density of filled states and free states at each side of energy barrier [34]. As the density of filled states at the c-Si/ SiO_2 interface is associated with (2), maximizing collecting carrier density improves the transport of carriers. In case of poly-Si CSCs, such an effect is achieved thanks to active dopants inside c-Si. It is worth noting that transport of carriers in poly-Si CSCs is deployed in the conduction (valence) band for n-type contact (p-type contact) featuring the so-called direct tunneling. The tunneling probability $\Gamma_e(r_{ox})$ is calculated by following Wentzel–Kramers–Brillouin approximation

$$\Gamma_e(r_{ox}) = \exp \left[-\frac{2}{\hbar} \int_0^{r_{ox}} \sqrt{2m_e (E_{f_e,n} - E_{C,cSi} - q\psi_e(r))} dr \right] \quad (4)$$

where \hbar is the reduced Planck constant and $\psi_e(r)$ is the electrostatic potential in terms of potential barrier profile along the position r for electrons, and m_e are the tunneling masses of electrons and holes. Technology computer-aided design (TCAD) Sentaurus considers a complex state-of-the-art model detailed in [45] and [52] to describe transport through heterointerfaces by tunneling. However, the purpose of this paper is to only identify parameters affecting the collection of carriers through tunneling oxide in poly-Si based CSCs. For this reason, we assume an exceptionally simplified thin oxide energy barrier as a rectangular barrier defined by a potential energy E_B and oxide thickness r_{ox} (see Fig. 1). With such an assumption, we account similar bandgap for poly-Si and c-Si. Then, (4) is simplified to

$$\Gamma_e(r_{ox}) = \exp \left[-\frac{2r_{ox}}{\hbar} \sqrt{2m_e (E_{Be} - E_{C,cSi})} \right] \quad (5)$$

Interestingly, r_{ox} , m_e , m_h , E_{Be} , and E_{Bh} have an exponential impact on $\Gamma_e(r_{ox})$, which contribute to define the current behavior [34], [45], [52] through G_e and G_h . From this approach, m_e , m_h , E_{Be} and E_{Bh} are the parameters inherent to the dielectric material used as tunneling oxide (uniform SiO_2), but r_{ox} is related to device process.

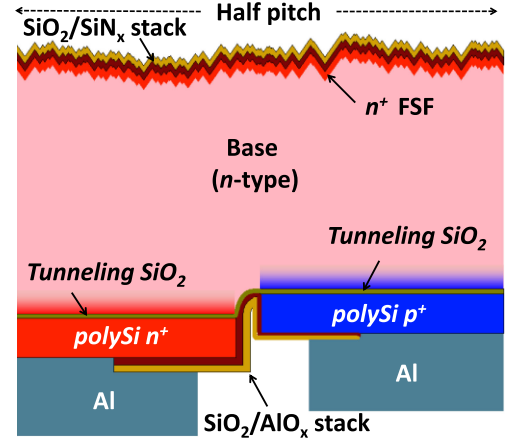


Fig. 2. Sketch of the simulation domain accurately describing the features of our IBC architecture [22], [53]. The absorber bulk is c-Si n-type. Front side is randomly textured and covered by thermal $\text{SiO}_2/\text{SiN}_x$ as ARC. The textured front side is passivated by a lowly doped FSF. The flat rear side consists of the n-type contact stack (SiO_2 /highly doped n-type poly-Si/Al) and the p-type contact stack (SiO_2 /highly doped p-type poly-Si/Al). Both contacts are separated by a gap consisting of quarter of $1\text{-}\mu\text{m}$ -wide radius circumference.

III. SIMULATION METHODOLOGY

Fig. 2 shows the two-dimensional (2-D) cross section of the poly-Si IBC solar cell symmetry element used to perform optoelectrical simulations. The model has been developed based on a reference IBC solar cell featuring a $280\text{-}\mu\text{m}$ thick, $5\text{-}\Omega\text{-cm}$ resistivity FZ c-Si n-type wafer and a $650\text{-}\mu\text{m}$ -wide pitch [22]. Consistent with processed device, the front interface is texturized by random pyramids and covered by a thermal SiO_2 and a SiN_x deposited by plasma enhanced chemical vapor deposition (PECVD) as anti-reflective coating (ARC).

Similar to [53], the front texturing was modeled by a sequence of triangles with a fixed base angle of 54.7° related to the wet-etching process, featuring a maximum height of $5.6\text{ }\mu\text{m}$. The rear hole- and electron-selective contact interfaces are planar and disconnected by a $1\text{-}\mu\text{m}$ -large curved gap that results from the self-aligned process [22]. To passivate the rear side of c-Si absorber bulk, a 1.5-nm -thick tunneling SiO_2 layer is formed by means of nitric acid oxidation of silicon [54]. The front surface field (FSF) is formed by phosphorus implantation. The n-type contact and the p-type contact are formed by 250-nm -thick low pressure chemical vapor deposition (LPCVD) poly-Si subsequently implanted with P and B, respectively [22], then annealed at $950\text{ }^\circ\text{C}$ and finally hydrogenated. Doping profiles were extracted from electrochemical capacitance measurements to obtain the doping profiles of the reference IBC solar cell [22].

A. Models and Parameters

The device model has been developed on finite element numerical simulator TCAD Sentaurus [52], according to the geometrical and physical parameters of the reference poly-Si IBC cell. The simulation approach is similar to the one described in [53]. Thus, the optical simulation is performed by using the internal ray-tracing model and free-carrier absorption (FCA) has been modeled assuming the doping concentration as carrier

TABLE I
SUMMARY OF PARAMETERS AND MODELS ASSUMED FOR SIMULATING
THE REFERENCE POLY-Si IBC SOLAR CELL

Parameter/Model	Value
Bulk resistivity	5 Ωcm
Substrate thickness	280 μm
Pitch	650 μm
Poly-Si thickness	250 nm [22]
SiO ₂ thickness	1.5 nm [22]
FSF doping peak	$1 \times 10^{19} \text{ cm}^{-3}$ [66]
n-contact doping	Doping profile ($1 \times 10^{20} \text{ cm}^{-3}$ [22])
p-contact doping	Doping profile ($1 \times 10^{20} \text{ cm}^{-3}$ [22])
Contact Resistance (measured TLM)	0.3 $\text{m}\Omega \cdot \text{cm}^2$ 0.9 $\text{m}\Omega \cdot \text{cm}^2$
Finger and bus bar resistance	Distributed model: 1.6 $\mu\Omega \cdot \text{cm}$
Tunneling Model	Non-local Tunneling model [52]
Effective tunneling masses for holes and electrons	$m_{\text{te}}=0.4 m_0$; $m_{\text{th}}=0.32 m_0$ [34] *

* m_0 is the electron rest mass. Doping profiles of n-type and p-type contacts are extended to c-Si according to [22].

concentration [55]. The electrical simulation is based on a drift-diffusion model, using state-of-the-art models [56], [57] for AM1.5G illumination [58]. It should be noted that optical and electrical simulation share the same simulation domain, then the 2-D optical generation rate obtained from the optical simulation is directly set into the electrical simulation stage [53].

A summary of parameters of the processed device used in this paper is presented in Table I.

The calibration of Shockley–Read–Hall (SRH) bulk and surface recombination parameters [bulk lifetime τ_{bulk} and surface recombination velocity (SRV)] were extracted from the validation process in which we compared simulated and measured current density–voltage (J – V) and external quantum efficiency (EQE) curves. Since our reference poly-Si IBC solar cell was processed at temperatures around 950 °C, we assume that the collection of carriers in poly-Si CSCs is characterized by tunneling mechanisms [28], [29]. These were modeled according to the non-local model implemented in TCAD Sentaurus [52].

B. Validation

The setup opto-electrical platform was used to simulate reflectance (R), EQE, transmittance (T), and J – V curves related to the real device. Accordingly, the device model was calibrated in terms of SRH parameters, which are not material dependent [53]. Fig. 3 shows the comparison between the measured and simulated R , T and EQE spectra. Similarly, Fig. 4 depicts the comparison between the measured and simulated J – V curves.

In general, we observed a good agreement between simulated and measured data in both spectral behavior and electrical characteristics, confirming that our simulation platform describes

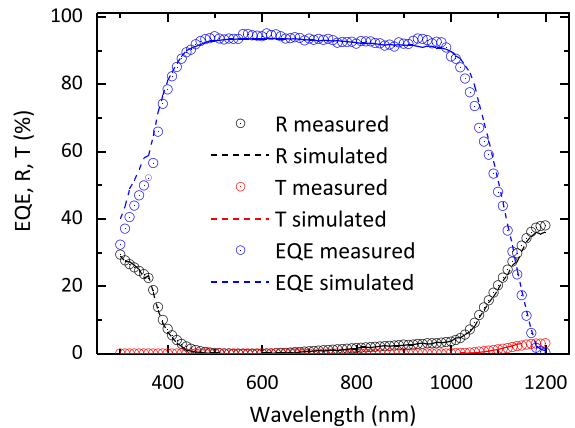


Fig. 3. Simulated and measured reflectance R , transmittance T , and EQE spectra of the reference poly-Si IBC solar cell.

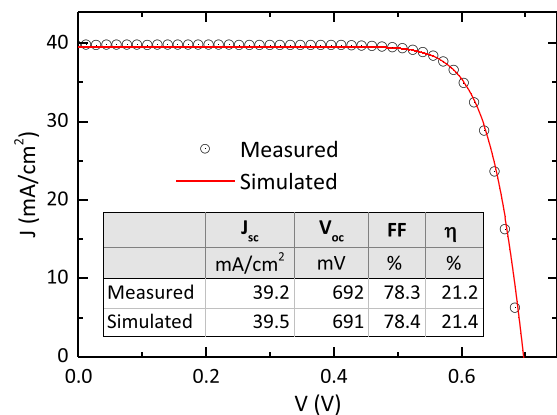


Fig. 4. Simulated and measured current density–voltage (J – V) characteristics of the reference poly-Si IBC. The inset table reports comparison between the extracted and measured external parameters.

accurately the physical mechanisms occurring in the reference device, including tunneling models.

IV. SIMULATION RESULTS

A. Optical and Electrical Loss Analysis

Resulting from the validation, we identified and extracted the main losses affecting the conversion efficiency of the reference device. These mechanisms were spectrally analyzed in the wavelength range between 300 and 1200 nm. We estimated R , T , free FCA and parasitic absorption in front SiN_x and in metallic contacts. Then, recombination losses were evaluated. Fig. 5 shows the quantification of optical and electrical losses for the reference poly-Si IBC solar cell. Considering AM 1.5G spectrum, every loss contribution was estimated in terms of implied current density (mA/cm^2). Main losses were due to recombination (2.41 mA/cm^2), reflectance (2.05 mA/cm^2), and FCA (1.33 mA/cm^2) [see Fig. 5(a)]. Looking into the recombination losses, they were mainly localized at front interface (41%) and c-Si bulk (51%) [see Fig. 5(b)].

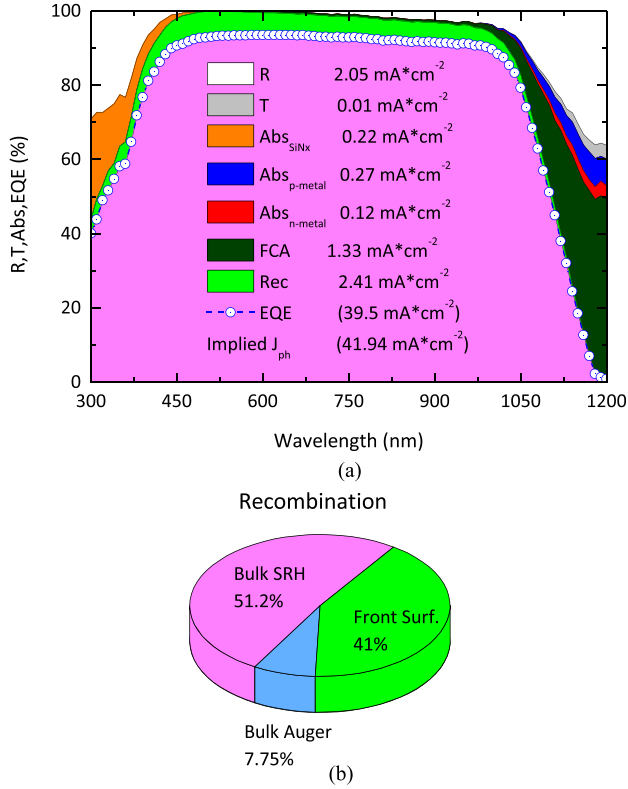


Fig. 5. (a) Estimated losses of the reference poly-Si IBC: reflectance R , transmittance T , FCA in c-Si and doped poly-Si layers, parasitic absorption (Abs) in front SiN_x layer and rear metallic contacts, and recombination (Rec.). Losses are reported in terms of mA/cm^2 . (b) Summary of the main recombination contributions.

TABLE II

SUMMARY OF EXTRACTED PARAMETERS FOR THE REFERENCE DEVICE AND ASSUMED PARAMETERS FOR EVALUATING THE IDEAL DEVICE

Parameter	Reference device [22]	Ideal device
SRH c-Si / n-type (p-type) contact interface SRV_n (SRV_p)	< 100 cm/s	0.1 cm/s
SRH Front surface recombination velocity (SRV_F)	5000 cm/s	0.1 cm/s (NO FSF)
SRH Bulk lifetime (τ_{bulk})	1.8 ms	10 ms

Table II summarizes the recombination parameters, allowing for model calibration. At n- and p-contact interface, such values match with those calculated from symmetrical samples [22]. However, it was revealed that main losses occur at the textured front interface ($\text{SRV}_F = 5000 \text{ cm/s}$). Considering the relatively low $J_{o,\text{FSF}} = 31 \text{ fA}/\text{cm}^2$ reported in [22] for a symmetrical test sample, this effect is ascribed to the introduction of interface defects during the patterning process. Improved the cleanliness of such process, to enhance the passivation quality at the textured front c-Si, a thin intrinsic amorphous silicon layer was deposited on top of the textured FSF followed by a SiN_x ARC layer. When compared with the solar cell used as a reference in this paper, a $\Delta J_{\text{sc}} = +1.5 \text{ mA}/\text{cm}^2$ was recorded, leading to a $+0.9\%_{\text{abs}}$ in conversion efficiency [5].

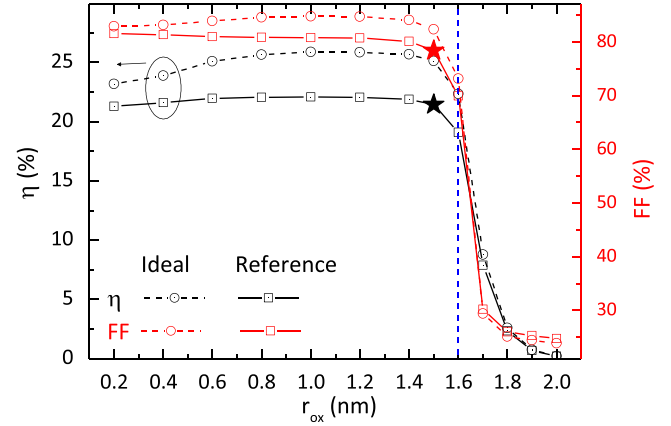


Fig. 6. Efficiency and FF of reference and ideal poly-Si IBC devices as a function of oxide thickness r_{ox} . Star symbols correspond to calibrated values from Section III.

After validating the opto-electrical platform and estimating main losses of the reference poly-Si IBC solar cell, we performed a set of simulations to identify the main parameters that influence and limit the performance of the reference device. Therefore, we kept constant parameters inherent to material properties in SiO_2 and poly-Si layers while we calculated the conversion efficiency as a function of the thin oxide thickness and of the rear geometry. Further, to assess recombination mechanisms, we estimated the influence of passivation quality at c-Si interfaces on solar cell performance.

The effect of each individual parameter was assessed by varying only one parameter at time and keeping constant the others according to Tables I and II. Additionally, to evaluate the potential performance of the solar cell, simulation results include two scenarios: reference device parameters, and almost ideal parameters but still realistic state-of-the-art technology (see Table II). Note that transport effects are quantified in terms of FF and recombination effects are apparent in terms of V_{oc} and J_{sc} values.

B. Transport

1) *Tunneling Oxide Thickness*: As mentioned in Section II, SiO_2 thickness r_{ox} exponentially influences the tunneling transport of carriers in terms of tunneling probability Γ in (3) and (5), (8), and (9). Such an effect is apparent in Fig. 6, depicting the strong degradation of FF and η when r_{ox} increases. A sharp efficiency decrease is observed for oxide thickness values larger than 1.6 nm. A reduction of r_{ox} from 1.6 to 1.5 nm improves efficiency by $2.5\%_{\text{abs}}$, while a further decrease of r_{ox} from 1.5 to 1 nm enhances the efficiency by another $0.7\%_{\text{abs}}$. As mentioned in Section II-B, the generation rate associated with tunneling (3) depends on the potential barrier size, the filled states, and the available states in both sides of such a barrier. The variation of tunneling oxide thickness affects not only the collection of collecting carriers, but also the transport of non-collecting carriers. Therefore, Fig. 6 reports that the conversion efficiency and FF are maximized for 1 nm r_{ox} . The decrease in efficiency for $r_{\text{ox}} < 1 \text{ nm}$ is explained in terms of less effective barrier for

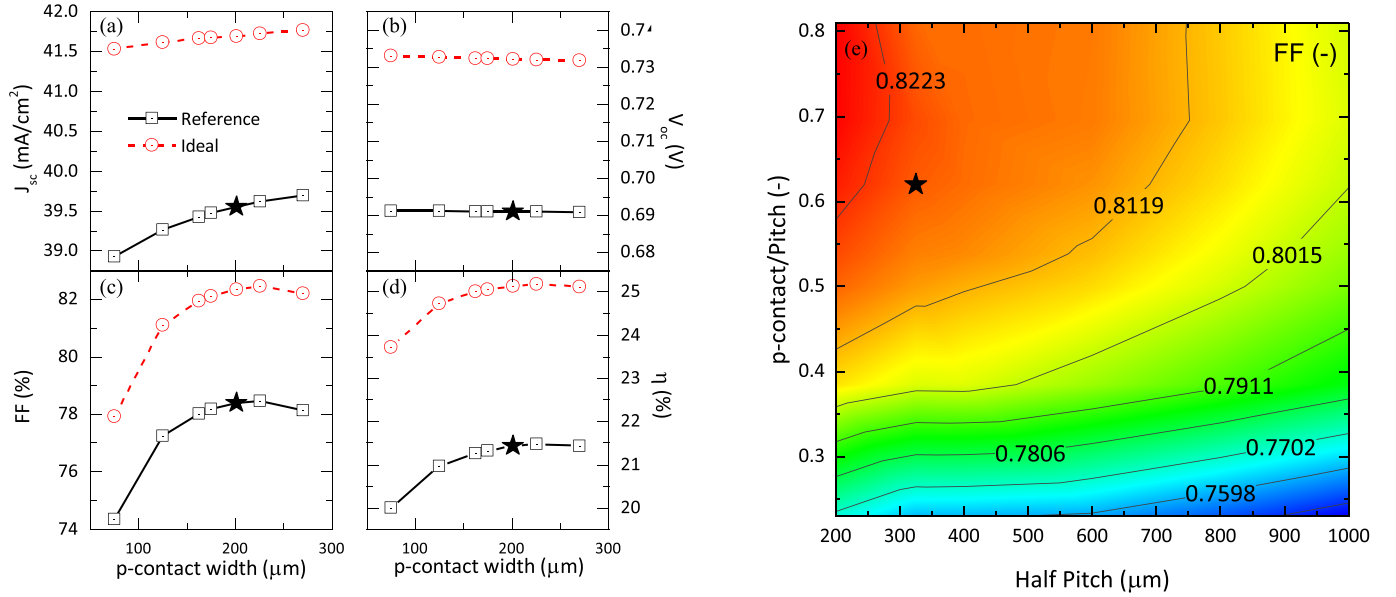


Fig. 7. External parameters: (a) J_{sc} , (b) V_{oc} , (c) FF, and (d) η of reference and ideal poly-Si IBC devices as a function of the p-type contact width. Stars symbols correspond to calibrated values from Section III. (e) Calculated FF of the ideal device as a function of half pitch and coverage of p-contact. Longer pitch values affect FF since carriers collecting path is increased. FF is optimal for p-contact over pitch around 70%.

non-collecting carriers. Indeed, reducing r_{ox} , contact passivation becomes less effective and carrier collection tends to be similar to homo-junction devices with lower V_{oc} . On the other hand, the decrease in efficiency for $r_{ox} > 1$ nm is explained by the reduced transport of collecting carriers in terms of lower tunneling probability. It is worth noting that for semiconductor applications r_{ox} thicknesses within 0.9 and 1.5 nm thickness are attainable depending on oxidation method [59], [60].

In general, higher η are achieved for 1-nm-thick r_{ox} due to the improvement of transport of collecting carriers through the energy barrier of the layer, keeping an effective barrier for transport of non-collecting carriers. This effect emphasizes the sensitivity of solar cell transport to SiO_2 thickness, becoming critical at 1.6 nm. In particular, a 1-nm-thick r_{ox} maximizes the conversion efficiency to 22.1%, assuming extracted recombination parameters, and to 25.9% considering ideal parameters case.

2) *Rear Geometry*: Typically IBC solar cells deal with lateral transport for collecting carriers [61]–[63] in terms of rear side geometry. Thus, to evaluate the impact of lateral transport on our poly-Si IBC device, we performed a set of simulations varying the p-type contact width, keeping constant the pitch and the connecting gap. In other words, smaller p-type contact fingers (emitter) entail a wider n-type contact fingers (back surface field) and vice versa. Simulations were run for a range of p-type contact (n-type contact) width from 150 to 440 μm (from 500 to 210 μm), assuming constant all the other parameters. Accordingly, the equivalent so-called p-type contact coverage is changed from 20% to 84%. Fig. 7 shows J_{sc} , V_{oc} , FF, and η as a function of p-type contact width for both the reference and the ideal poly-Si IBC devices. In general, the so-called *electrical shadowing* effect for homo-junction IBC solar cells [62], [64] is almost negligible as J_{sc} and V_{oc} trends demonstrate in Fig. 7(a) and (b) in case of the ideal device. Indeed, differently

than IBC homo-junction solar cells, IBCs with CSC feature similar passivation for both contacts, then J_{sc} and V_{oc} are almost independent from rear side geometry. However, it is worth noting that in case of the reference device, recombination effect becomes apparent in J_{sc} , thanks to the dominant front recombination calculated for reference device (see Table II). Interestingly, a bell-shaped curve is observed in FF case featuring a clear maximum value at 78.4% (82.4%) for a p-type contact width of 452 μm (or 69% pitch coverage) for reference (ideal) device. Such a trend reveals transport issues occurring in thin oxide layer as a result of crowded tunneling current in case of electrons for smaller n-type contact width and crowded tunneling of holes in case of small p-type contact. Hence, the maximum FF results from the tradeoff between tunneling currents of electrons and holes in terms of optimal p-type contact coverage. Looking into Fig. 7(c) and (d), the trend of FF dictates that of η , which tops at 21.5% (25.2%) for the p-type contact width value 452 μm (70% of p-contact coverage in case of both reference and ideal devices). Such a trend is reported in detail in Fig. 7(e) for FF evaluated for different pitch values and p-contact over pitch coverage. In fact, the FF is optimal for p-contact over the pitch coverage of 70%. Similar to c-Si IBC homo-junction and heterojunction solar cells [50], [53], [62], [63], small pitch values increase FF.

C. Passivation Quality

In this section, the effect of passivation quality on solar cell performance is investigated. To do so, we evaluated V_{oc} and η as functions of SRV at the p-type contact (SRV_p), n-type contact (SRV_n), and front (SRV_F). It is worth noting that SRV is related to defects at c-Si interface and can be reduced depending on interface treatment to values below 1 cm/s [65].

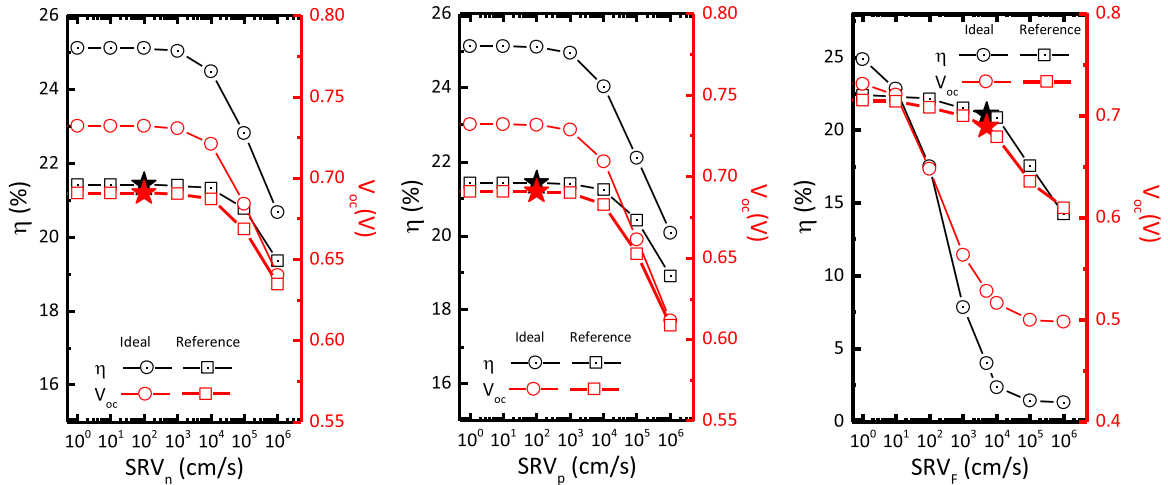


Fig. 8. η and V_{oc} as a function of SRV at n-type contact (left), p-type contact (center), and textured front (right) interfaces. Stars symbols correspond to calibrated values from Section III.

In each case, we varied the SRV in the range between 0.1 and 1×10^6 cm/s (see Fig. 8). In case of n-type and p-type contact interfaces (see Fig. 8 left and center), a similar behavior is observed. The V_{oc} and η of the reference (ideal) device are almost constant close to maximum values at 690 (732) mV and 21.4% (25.15%) for SRV values lower than 1×10^4 cm/s. However, for SRV values larger than 1×10^4 cm/s, V_{oc} and η strongly decrease. This effect is ascribed to the doping profile that extends inside c-Si [22], thus inducing an electrical field passivation [62] that is effective for SRV values up to 1×10^4 cm/s. Similarly, in case of textured front c-Si interface, the reference device features an implanted doping profile that sets up a high–low homojunction. This induces an electric field passivation that keeps V_{oc} and η from massively decreasing for SRV_F values up to 1×10^3 cm/s [66]. For SRV_F values beyond such a threshold, V_{oc} and η strongly decrease. Such a trend is different in case of the ideal device. In fact, in absence of FSF, V_{oc} and η strongly depend on SRV_F [53], allowing high performance only for SRV_F value in the range of 1 cm/s. After this sensitivity analysis, the estimated maximum conversion efficiency is limited to 22.38% for the reference device, while it is 25.2% for the ideal device with no-FSF. This difference is mainly caused by the presence of doped FSF in the reference IBC device that increases the intrinsic recombination as a drawback if SRV_F is lower than 10 cm/s [see Fig. 8(c)].

D. Performance Limit

In this section, we performed an optimization study of poly-Si-based IBC solar cell. Accordingly, we considered the parameters of the ideal device (see Table II) featuring $r_{ox} = 1$ nm. This way we reduce the potential barrier and, therefore, improve the transport of carriers through the SiO_2 layer. With this assumption, $\eta = 25.9\%$ (see Fig. 6) was calculated. However, the in-diffused doping profile exceeds the doping peak value that maximizes the carrier concentration at interface as discussed in Section II. Indeed, measured doping peak concentration is

1×10^{20} cm $^{-3}$ [22] while required values are 3.2×10^{19} cm $^{-3}$ for donors (n-type contact) and 1.8×10^{19} cm $^{-3}$ for acceptors (p-type contact). In this condition, both selectivity and Auger recombination are enhanced; therefore, a precise doping profile has to be enforced. In this respect, a shallow Gaussian doping profile with 50-nm-deep junction and doping peak 2×10^{19} cm $^{-3}$ was assumed as optimal, resulting in $\eta = 26.3\%$ (Optimized design #1 in Table III).

This device is limited by intrinsic recombination in the absorber bulk. To reduce intrinsic recombination, two alternatives are possible: increase bulk resistivity (reduce doping) and/or reduce bulk thickness. To keep the same bulk resistivity with respect to the reference device, we analyzed the impact of the thickness of the absorber bulk on η , J_{sc} and V_{oc} for both Al and Ag as rear contact materials. Looking at the top panel of Fig. 9, J_{sc} increases as the bulk thickness increases while V_{oc} decreases. When the bulk thickness increases, the enhancement in J_{sc} is attributed to the rise of absorbed photons while the V_{oc} degradation is due to the increase of intrinsic recombination. While the trend of V_{oc} is not affected by different back reflectors, the trend of J_{sc} in case of Ag contact is sensibly higher than the counterpart based on Al. Thus, the V_{oc} contribution dominates the trend of conversion efficiency, but the choice of the rear contact material sets the absolute η values. In our study, we did not simulate solar cells based on wafers thinner than 100 μ m for two main reasons. First, our optical simulation framework might require additional calibration due to the multiple reflection correction reported in [53]. Second, pursuing high efficiency for wafers thinner than 100 μ m is currently not industrially relevant [1] and might negatively affect the FF of manufactured devices owing to mechanical stress [8]. Thus, we considered that 100 μ m is the bulk thickness that maximizes the efficiency (Optimized design #2 in Table III), exhibiting $V_{oc} = 754$ mV. Such V_{oc} value is around 7 mV lower than c-Si V_{oc} limit [67] due to intrinsic recombination associated with doping on bulk and buried doping profiles at contact interfaces. Besides, as anticipated, the effect of switching the rear reflector from Al to

TABLE III
 COMPARISON BETWEEN OPTIMIZED POLY-Si IBC SOLAR CELL DESIGNS

Parameter	Optimized Design #1	Optimized Design #2	Optimized Design #3	Optimized Design #4	Optimized Design #5
p-contact finger width (μm)	452	452	452	452	452
n-contact finger width (μm)	198	198	198	198	198
Pitch (μm)	650	650	650	650	650
r_{ox} (nm)	1	1	1	1	1
Substrate thickness (μm)	280	100	100	100	100
Poly-Si thickness (nm)	250	250	250	20	20
Metal contact	Al	Al	Ag	Ag	Ag
Bulk lifetime (ms)	10	10	10	10	10
ARC	SiNi _x (60 nm) SiO ₂ (15 nm)	MgF₂ (100 nm) SiNi _x (50 nm) SiO ₂ (10 nm)			
J_{sc} (mA/cm ²)	42	40.9	41.2	41.5	41.7
V_{oc} (mV)	735	754	754	754	754.1
FF (%)	85.2	86.6	86.6	86.7	86.7
η (%)	26.3	26.7	26.9	27.1	27.3

Optimized design #1 shows the best calculated efficiency in the same process framework of the fabricated reference device, #2 refers to optimization allowing different bulk thickness, #3 refers to contact material, #4 refers to optimized metal contact patterning and poly-Si thickness, and #5 refers to double ARC.

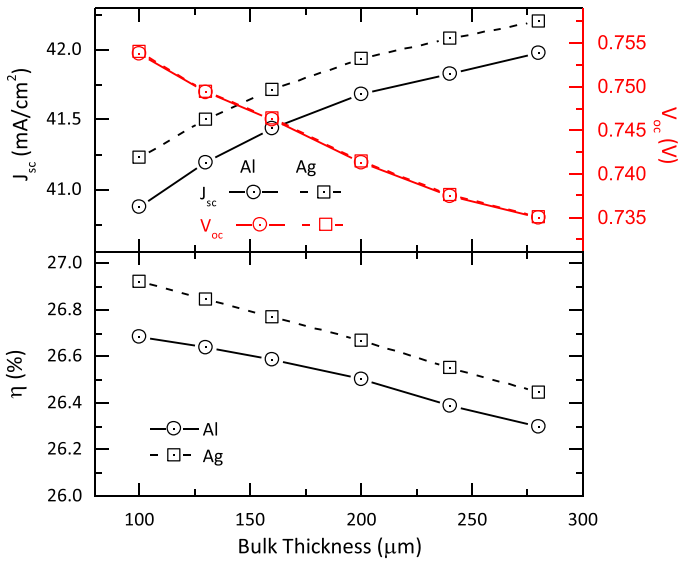


Fig. 9. Potential J_{sc} and V_{oc} (top) and η (bottom) of IBC poly-Si cell for different bulk thickness and Ag or Al as metal contacts accounting for ideal device parameters (see Table II).

Ag increases the J_{sc} value by 0.3 mA/cm^2 and η by $0.25\%_{\text{abs}}$, leading to $\eta = 26.9\%$ (Optimized design #3 in Table III).

To further improve the conversion efficiency aiming at reducing FCA losses, we carried out a set of simulations to optimize the poly-Si thickness (r_{poly}) and metal contact coverage. The optimization process was deployed according to [53]. In general, by decreasing r_{poly} , J_{sc} is improved due to FCA losses reduction, but the lateral transport losses in the poly-Si

increase. However, lateral transport in poly-Si depends also on the contact coverage that it is linked to metal parasitic absorption. In fact, within this optimization process, three competitive mechanisms are identified. The first is that FCA decreases by decreasing poly-Si thickness. The second is that lateral transport loss decreases by increasing metal contact. The third is that metal parasitic absorption increases by increasing metal contact. The optimization process resulted in $\Delta J_{\text{sc}} = +0.25 \text{ mA/cm}^2$ and $\eta = 27.1\%$ for a 20-nm-thick poly-Si thickness and 80% contact coverage (Optimized design #4 in Table III). We note that in case of using oxide thickness thicker than 1 nm and up to 1.6 nm, optimized J_{sc} and V_{oc} values remain, but FF changes as reported in Fig. 6, since the performance of the device becomes limited by transport through tunneling oxide.

At this point, optical losses can be potentially reduced by applying a more advanced double ARC [68]. Deploying an additional 100-nm-thick MgF₂ layer [69], [70] on the standard SiN_x, we improved the J_{sc} of our simulated poly-Si IBC device by 0.23 mA/cm^2 . The optimized design #5 in Table III summarizes the best external parameters found in this paper: $J_{\text{sc}} = 41.7 \text{ mA/cm}^2$, $V_{\text{oc}} = 754 \text{ mV}$, FF = 86.7%, and $\eta = 27.3\%$. Interestingly, similar values are calculated for optimized IBC solar cells with SHJ scheme [50], thus revealing similar potential performance for both type of CSCs. After this optimization process, we note a clear reduction of recombination losses that improves both V_{oc} and J_{sc} . On the other hand, pure optical losses ($R + T$ and $\text{Abs}_{\text{parasitic}}$) are essentially unaltered even for the optimized 100- μm -thick bulk (see Fig. 10). In fact, if the dual ARC quenches primary reflectance, the deployment of Ag rear reflector, together with thinner bulk, increases the rear

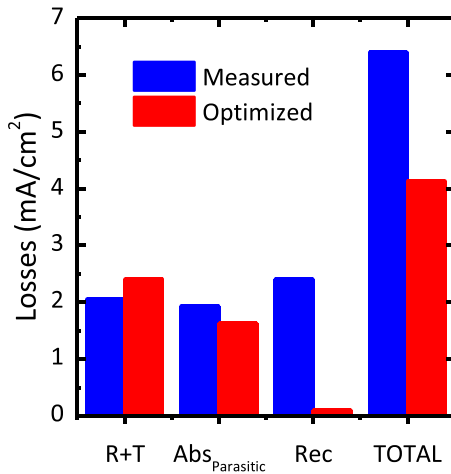


Fig. 10. Comparison of losses mechanisms between the measured poly-Si IBC solar cell and the poly-Si IBC device fully optimized based on parameters reported in Table III (optimized design #5).

reflectance, augmenting the chance for long wavelength light to escape the device. At the same time, thinner doped poly-Si layers not only drastically decrease the FCA, but also enable Ag to absorb more light parasitically.

V. CONCLUSION

The impact of main process-related parameters on the performance of IBC solar cells featuring poly-Si CSCs was studied here. Carrier selectivity and tunneling concepts were used to identify the parameters affecting transport in terms of FF. It was identified that carrier density at c-Si/SiO₂ interface together with oxide thickness affects the collection of carriers. For an efficient transport, carrier concentrations at interface are supported by in-diffused dopants from highly doped poly-Si layers resulting from a high-temperature process. Our simulation framework based on TCAD Sentaurus was validated by comparing the measured R , T , and EQE spectra, and electrical parameters of a reference device. As result of the calibration process, the opto-electrical losses were quantitatively and qualitatively identified. Main losses were related to recombination, of which 41% due to the front surface and 51% due to the bulk. The calibrated model was afterward devoted to analyzing the impact of process parameters on the performance of our reference IBC device. The parameters under study were SiO₂ thickness, rear side geometry, and passivation quality at front and rear surfaces. Aiming at exploring the potential conversion efficiency of our architecture, we looked at both the reference device and an ideal device, featuring outstanding bulk lifetime and passivation quality ($\tau_{\text{bulk}} = 10$ ms and SRV = 0.1 cm/s) with no FSF. Simulation results revealed that SiO₂ thickness beyond 1.6 nm forbids to achieve high efficiency, due to transport degradation ascribed to the strong decrease in tunneling probability of collecting carriers. Indeed, SiO₂ thickness < 1.6 nm improves the transport of collecting carriers. On the other hand, SiO₂ thickness < 1 nm enables also the transport of non-collecting carriers, thus increasing contact recombination. Therefore, we identified an optimum oxide thickness of 1 nm that allows the tunneling of collecting carriers while still

concurrently restricting tunneling of non-collecting carriers. For 1-nm-thick SiO₂, $\eta = 25.9\%$ was calculated. Additionally, we observed that the efficiency curve as a function of emitter width exhibits a bell shape with a clear maximum value for a p-type contact width over a pitch ratio of 69%. We also found that the n-type contact, p-type contact, and FSF doping profiles inside c-Si enhance the electrical field passivation. Therefore, V_{oc} and η are almost insensitive to SRV values up to 1×10^4 cm/s in case of n-type and p-type contact and up to 1×10^3 cm/s in case of FSF. Keeping 1-nm-thick tunneling SiO₂, engineering the doping profile of both emitter and BSF and switching from 280 to 100- μm -thick bulk, the calculated potential conversion efficiency was raised to 26.7%. Following further optimizations that touched upon poly-Si thickness (20 nm), metal contact material (Ag), metallization fraction (80%), and double ARC (SiN_x/MgF₂), an ultimate efficiency of 27.3% was simulated.

Our simulation methodology assumes that transport through uniform thin SiO₂ layer is exclusively described by tunneling concepts neglecting pinhole-transport contribution. In particular, the followed modeling approach has been successfully deployed for the design of advanced semiconductor devices and related processes. In this paper, we have not performed extensive experimental characterization to assess the applicability of contradicting transport models (tunneling, pinholes or both). Accordingly, presented results should be interpreted considering this assumption in mind.

REFERENCES

- [1] ITRPV, "International technology roadmap for photovoltaic (ITRPV)," Frankfurt, Germany, 2018.
- [2] C. Battaglia, A. Cuevas, and S. De Wolf, "High-efficiency crystalline silicon solar cells: Status and perspectives," *Energy Environ. Sci.*, vol. 9, pp. 1552–1576, 2016.
- [3] F. Haase *et al.*, "Laser contact openings for local poly-Si-metal contacts enabling 26.1%-efficient POLO-IBC solar cells," *Sol. Energy Mater. Sol. Cells*, vol. 186, pp. 184–193, Nov. 2018.
- [4] C. Reichel, F. Granek, M. Hermle, and S. W. Glunz, "Back-contacted back-junction n-type silicon solar cells featuring an insulating thin film for decoupling charge carrier collection and metallization geometry," *Prog. Photovolt. Res. Appl.*, vol. 21, no. 5, pp. 1063–1076, Mar. 2013.
- [5] G. Yang *et al.*, "High-efficiency black IBC c-Si solar cells with poly-Si as carrier-selective passivating contacts," *Sol. Energy Mater. Sol. Cells*, vol. 186, pp. 9–13, Nov. 2018.
- [6] A. Tomasi *et al.*, "Simple processing of back-contacted silicon heterojunction solar cells using selective-area crystalline growth," *Nature Energy*, vol. 2, Apr. 2017, Art. no. 17062.
- [7] P. J. Cousins *et al.*, "Generation 3: Improved performance at lower cost," in *Proc. Conf. Rec. IEEE Photovolt. Spec. Conf.*, 2010, pp. 275–278.
- [8] K. Yoshikawa *et al.*, "Silicon heterojunction solar cell with interdigitated back contacts for a photoconversion efficiency over 26%," *Nature Energy*, vol. 2, no. 3, Mar. 2017, Art. no. 17032.
- [9] E. Franklin *et al.*, "Design, fabrication and characterisation of a 24.4% efficient interdigitated back contact solar cell," *Prog. Photovolt. Res. Appl.*, vol. 24, no. 4, pp. 411–427, Apr. 2016.
- [10] N. Guerra, R. De Rose, M. Guevara, P. Procel, M. Lanuzza, and F. Crupi, "Understanding the impact of point-contact scheme and selective emitter in a c-Si BC-BJ solar cell by full 3D numerical simulations," *Sol. Energy*, vol. 155, pp. 1443–1450, Oct. 2017.
- [11] M. Zanucoli, P. Magnone, E. Sangiorgi, and C. Fiegna, "Analysis of the impact of geometrical and technological parameters on recombination losses in interdigitated back-contact solar cells," *Sol. Energy*, vol. 116, pp. 37–44, Jun. 2015.
- [12] F. Haase *et al.*, "Perimeter recombination in 25%-efficient IBC solar cells with passivating POLO contacts for both polarities," *IEEE J. Photovolt.*, vol. 8, no. 1, pp. 23–29, Jan. 2017.

- [13] G. Nogay *et al.*, "Interplay of annealing temperature and doping in hole selective rear contacts based on silicon-rich silicon-carbide thin films," *Sol. Energy Mater. Sol. Cells*, vol. 173, pp. 18–24, Dec. 2017.
- [14] A. Richter, J. Benick, F. Feldmann, A. Fell, M. Hermle, and S. W. Glunz, "n-Type Si solar cells with passivating electron contact: Identifying sources for efficiency limitations by wafer thickness and resistivity variation," *Sol. Energy Mater. Sol. Cells*, vol. 173, pp. 96–105, 2017.
- [15] B. Paviet-Salomon *et al.*, "Interdigitated back contact silicon heterojunction solar cells featuring an interband tunnel junction enabling simplified processing," *Sol. Energy*, vol. 175, pp. 60–67, Feb. 2018.
- [16] L. Mazzarella *et al.*, "Nanocrystalline silicon emitter optimization for Si-HJ solar cells: Substrate selectivity and CO₂ plasma treatment effect," *Phys. Status Solidi*, vol. 214, no. 2, 2017, Art. no. 1532958.
- [17] K. Masuko *et al.*, "Achievement of more than 25% conversion efficiency with crystalline silicon heterojunction solar cell," *IEEE J. Photovolt.*, vol. 4, no. 6, pp. 1433–1435, Nov. 2014.
- [18] A. Moldovan, F. Feldmann, M. Zimmer, J. Rentsch, J. Benick, and M. Hermle, "Tunnel oxide passivated carrier-selective contacts based on ultra-thin SiO₂ layers," *Sol. Energy Mater. Sol. Cells*, vol. 142, pp. 123–127, Nov. 2015.
- [19] C. Reichel *et al.*, "Tunnel oxide passivated contacts formed by ion implantation for applications in silicon solar cells," *J. Appl. Phys.*, vol. 118, no. 20, 2015, Art. no. 205701.
- [20] M. Rienacker *et al.*, "Junction resistivity of carrier-selective polysilicon on oxide junctions and its impact on solar cell performance," *IEEE J. Photovolt.*, vol. 7, no. 1, pp. 11–18, Jan. 2017.
- [21] F. Feldmann, C. Reichel, R. Müller, and M. Hermle, "The application of poly-Si/SiO_x contacts as passivated top/rear contacts in Si solar cells," *Sol. Energy Mater. Sol. Cells*, vol. 159, pp. 265–271, 2017.
- [22] G. Yang, A. Ingenito, O. Isabella, and M. Zeman, "IBC c-Si solar cells based on ion-implanted poly-silicon passivating contacts," *Sol. Energy Mater. Sol. Cells*, vol. 158, pp. 84–90, 2016.
- [23] J. Stuckelberger *et al.*, "Recombination analysis of phosphorus-doped nanostructured silicon oxide passivating electron contacts for silicon solar cells," *IEEE J. Photovolt.*, vol. 8, no. 2, pp. 389–396, Mar. 2018.
- [24] G. Nogay *et al.*, "Silicon-rich silicon carbide hole-selective rear contacts for crystalline-silicon-based solar cells," *ACS Appl. Mater. Interfaces*, vol. 8, pp. 35660–35667, 2016.
- [25] G. Yang, P. Guo, P. Procel, A. Weeber, O. Isabella, and M. Zeman, "Polycrystalline silicon-oxide films as carrier-selective passivating contacts for c-Si solar cells," *Appl. Phys. Lett.*, vol. 112, no. 19, May 2018, Art. no. 193904.
- [26] R. Peibst *et al.*, "Working principle of carrier selective poly-Si/c-Si junctions: Is tunnelling the whole story?" *Sol. Energy Mater. Sol. Cells*, vol. 158, pp. 60–67, 2016.
- [27] T. F. Wietler *et al.*, "Pinhole density and contact resistivity of carrier selective junctions with polycrystalline silicon on oxide," *Appl. Phys. Lett.*, vol. 110, no. 25, 2017, Art. no. 253902.
- [28] H. Steinkemper, F. Feldmann, M. Bivour, and M. Hermle, "Numerical simulation of carrier-selective electron contacts featuring tunnel oxides," *IEEE J. Photovolt.*, vol. 5, no. 5, pp. 1348–1356, Sep. 2015.
- [29] F. Feldmann *et al.*, "Charge carrier transport mechanisms of passivating contacts studied by temperature-dependent J-V measurements," *Sol. Energy Mater. Sol. Cells*, vol. 178, pp. 15–19, 2018.
- [30] A. Liu *et al.*, "Direct observation of the impurity gettering layers in polysilicon-based passivating contacts for silicon solar cells," *ACS Appl. Energy Mater.*, vol. 1, pp. 2275–2282, 2018.
- [31] A. Moldovan *et al.*, "Tunnel oxide passivated carrier-selective contacts based on ultra-thin SiO₂ layers grown by photo-oxidation or wet-chemical oxidation in ozonized water," in *Proc. IEEE 42nd Photovolt. Spec. Conf.*, 2015, vol. 142, pp. 123–127.
- [32] D. Yan, A. Cuevas, Y. Wan, and J. Bullock, "Passivating contacts for silicon solar cells based on boron-diffused recrystallized amorphous silicon and thin dielectric interlayers," *Sol. Energy Mater. Sol. Cells*, vol. 152, pp. 73–79, 2016.
- [33] D. Yan, A. Cuevas, J. Bullock, Y. Wan, and C. Samundsett, "Phosphorus-diffused polysilicon contacts for solar cells," *Sol. Energy Mater. Sol. Cells*, vol. 142, pp. 75–82, 2015.
- [34] A. Gehring and S. Selberherr, "Modeling of tunneling current and gate dielectric reliability for nonvolatile memory devices," *IEEE Trans. Device Mater. Reliab.*, vol. 4, no. 3, pp. 306–319, Sep. 2004.
- [35] H. Watanabe, D. Matsushita, and K. Muraoka, "20 Determination of tunnel mass and thickness of gate oxide including poly-Si / SiO₂ and Si / SiO₂ interfacial transition layers," *IEEE Trans. Electron Devices*, vol. 53, no. 6, pp. 1323–1330, Jul. 2004.
- [36] A. Schenk and G. Heiser, "Modeling and simulation of tunneling through ultra-thin gate dielectrics," *J. Appl. Phys.*, vol. 81, no. 12, pp. 7900–7908, 1997.
- [37] H. Y. Yang, H. Niimi, and G. Lucovsky, "Tunneling currents through ultra-thin oxide/nitride dual layer gate dielectrics for advanced microelectronic devices," *J. Appl. Phys.*, vol. 83, no. 4, pp. 2327–2337, 1998.
- [38] B. Brar, G. D. Wilk, and a. C. Seabaugh, "Direct extraction of the electron tunneling effective mass in ultrathin SiO₂," *Appl. Phys. Lett.*, vol. 69, no. 18, 1996, Art. no. 2728.
- [39] Y. C. Yeo, T. J. King, and C. Hu, "Direct tunneling leakage current and scalability of alternative gate dielectrics," *Appl. Phys. Lett.*, vol. 81, no. 11, pp. 2091–2093, 2002.
- [40] E. M. Vogel *et al.*, "Modeled tunnel currents for high dielectric constant dielectrics," *IEEE Trans. Electron Devices*, vol. 45, no. 6, pp. 1350–1355, Jun. 1998.
- [41] M. Nicolai, M. Zanucoli, F. Feldmann, M. Hermle, and C. Fiegna, "Analysis of silicon solar cells with poly-Si/SiO_x carrier-selective base and emitter contacts," *IEEE J. Photovolt.*, vol. 8, no. 1, pp. 103–109, Jan. 2018.
- [42] M. Rienacker *et al.*, "Junction resistivity of carrier-selective polysilicon on oxide junctions and its impact on solar cell performance," *IEEE J. Photovolt.*, vol. 7, no. 1, pp. 11–18, Jan. 2017.
- [43] R. Peibst *et al.*, "Building blocks for industrial, screen-printed double-side contacted POLO cells with highly transparent ZnO:Al layers," *IEEE J. Photovolt.*, vol. 8, no. 3, pp. 719–725, May 2018.
- [44] F. Li, S. Mudanai, and Y. Fan, "Compact model of MOSFET electron tunneling current through ultra-thin SiO₂ and high-k gate stacks," *Device Res.*, vol. 24, pp. 47–48, 2003.
- [45] MeiKei Jeong, P. M. Solomon, S. E. Laux, H.-S. P. Wong, and D. Chidambarrao, "Comparison of raised and Schottky source/drain MOSFETs using a novel tunneling contact model," in *Proc. Int. Electron Devices Meet. Tech. Dig.*, 1998, pp. 733–736.
- [46] H. Yu, Y. T. Hou, M. F. Li, and D. L. Kwong, "Investigation of hole-tunneling current through ultrathin oxynitride/oxide stack gate dielectrics in p-MOSFETs," *IEEE Trans. Electron Devices*, vol. 49, no. 7, pp. 1158–1164, Jul. 2002.
- [47] F. Feldmann *et al.*, "Charge carrier transport mechanisms of passivating contacts studied by temperature-dependent J-V measurements," *Sol. Energy Mater. Sol. Cells*, vol. 178, pp. 15–19, May 2018.
- [48] N. Folchert, M. Rienacker, A. A. Yeo, B. Min, R. Peibst, and R. Brendel, "Temperature-dependent contact resistance of carrier selective Poly-Si on oxide junctions," *Sol. Energy Mater. Sol. Cells*, vol. 185, pp. 425–430, 2018.
- [49] R. Brendel and R. Peibst, "Contact selectivity and efficiency in crystalline silicon photovoltaics," *IEEE J. Photovolt.*, vol. 6, no. 6, pp. 1413–1420, Nov. 2016.
- [50] P. Procel, G. Yang, O. Isabella, and M. Zeman, "Theoretical evaluation of contact stack for high efficiency IBC-SHJ solar cells," *Sol. Energy Mater. Sol. Cells*, vol. 186, pp. 66–77, Nov. 2018.
- [51] A. Fell *et al.*, "Input parameters for the simulation of silicon solar cells in 2014," *IEEE J. Photovolt.*, vol. 5, no. 4, pp. 1250–1263, Jul. 2015.
- [52] Synopsis, "Sentaurus device user," p. 2009, 2013.
- [53] P. Procel *et al.*, "Opto-electrical modelling and optimization study of a novel IBC c-Si solar cell," *Prog. Photovolt. Res. Appl.*, vol. 25, no. 6, pp. 452–469, Jun. 2017.
- [54] G. Yang, A. Ingenito, N. Van Hameren, O. Isabella, and M. Zeman, "Design and application of ion-implanted polysi passivating contacts for interdigitated back contact c-Si solar cells," *Appl. Phys. Lett.*, vol. 108, no. 3, 2016, Art. no. 033903.
- [55] S. C. Baker-Finch, K. R. McIntosh, D. Yan, K. C. Fong, and T. C. Kho, "Near-infrared free carrier absorption in heavily doped silicon," *J. Appl. Phys.*, vol. 116, no. 6, 2014, Art. no. 063106.
- [56] A. Fell *et al.*, "Input parameters for the simulation of silicon solar cells in 2014," *IEEE J. Photovolt.*, vol. 5, no. 4, pp. 1250–1263, Jul. 2015.
- [57] P. P. Altermatt, "Models for numerical device simulations of crystalline silicon solar cells—a review," *J. Comput. Electron.*, vol. 10, no. 3, pp. 314–330, 2011.
- [58] *Standard tables for reference solar spectral irradiances: Direct normal and hemispherical on 37° tilted surface*, ASTM G173-03, 2012.
- [59] B. Stegemann *et al.*, "Ultra-thin silicon oxide layers on crystalline silicon wafers: Comparison of advanced oxidation techniques with respect to chemically abrupt SiO₂/Si interfaces with low defect densities," *Appl. Surf. Sci.*, vol. 395, pp. 78–85, 2017.
- [60] M. Koh *et al.*, "Limit of gate oxide thickness scaling in MOSFETs due to apparent threshold voltage fluctuation induced by tunnel leak-

age current," *IEEE Trans. Electron Devices*, vol. 48, no. 2, pp. 259–264, Feb. 2001.

- [61] F. Granek, M. Hermle, D. M. Huljić, O. Schultz-Wittmann, and S. W. Glunz, "Enhanced lateral current transport via the front N + diffused layer of n-type high-efficiency back-junction back-contact silicon solar cells," *Prog. Photovolt. Res. Appl.*, vol. 17, no. 1, pp. 47–56, Jan. 2009.
- [62] P. Procel *et al.*, "Numerical simulation of the impact of design parameters on the performance of back-contact back-junction solar cell," *J. Comput. Electron.*, vol. 15, no. 1, pp. 260–268, Mar. 2016.
- [63] S. Kluska, F. Granek, M. Rüdiger, M. Hermle, and S. W. Glunz, "Modeling and optimization study of industrial n-type high-efficiency back-contact back-junction silicon solar cells," *Sol. Energy Mater. Sol. Cells*, vol. 94, no. 3, pp. 568–577, 2010.
- [64] C. Reichel, F. Granek, M. Hermle, and S. W. Glunz, "Investigation of electrical shading effects in back-contacted back-junction silicon solar cells using the two-dimensional charge collection probability and the reciprocity theorem," *J. Appl. Phys.*, vol. 109, no. 2, 2011, Art. no. 024507.
- [65] A. Richter, S. W. Glunz, F. Werner, J. Schmidt, and A. Cuevas, "Improved quantitative description of Auger recombination in crystalline silicon," *Phys. Rev. B*, vol. 86, no. 16, 2012, Art. no. 165202.
- [66] A. Ingenito, O. Isabella, and M. Zeman, "Simplified process for high efficiency, self-aligned IBC c-Si solar cells combining ion implantation and epitaxial growth: Design and fabrication," *Sol. Energy Mater. Sol. Cells*, vol. 157, pp. 354–365, 2016.
- [67] A. Richter, M. Hermle, and S. W. Glunz, "Reassessment of the limiting efficiency for crystalline silicon solar cells," *IEEE J. Photovolt.*, vol. 3, no. 4, pp. 1184–1191, Oct. 2013.
- [68] H. Steinkemper, F. Feldmann, M. Bivour, and M. Hermle, "Theoretical investigation of carrier-selective contacts featuring tunnel oxides by means of numerical device simulation," *Energy Procedia*, vol. 77, pp. 195–201, 2015.
- [69] K. McIntosh, M. Abbott, and B. Sudbury, "PVLighthouse." [Online]. Available: <https://www2.pvlighthouse.com.au/resources/photovoltaic-materials/refractiveindex/refractiveindex.aspx>. Accessed on: Nov. 5, 2016.
- [70] M. J. Dodge, "Refractive properties of magnesium fluoride," *Appl. Opt.*, vol. 23, no. 12, pp. 1980–1985, 1984.



Paul Procel received the Ph.D. degree from the University of Calabria, Rende, Italy, in 2017, for his research in numerical simulations of advanced silicon solar cells.

In 2015, for an internship, he joined the Photovoltaic Materials and Devices Group, Delft University of Technology, Delft, The Netherlands, where he worked on advanced opto-electrical simulations of interdigitated back contacted solar cells. Since 2017, he has been with the Delft University of Technology as a Postdoctoral Researcher focusing on design and

development of silicon heterojunction solar cells. His research interests include opto-electrical simulations and design of solar cells and semiconductor devices.



Guangtao Yang received the Ph.D. degree from the Delft University of Technology, Delft, The Netherlands, in 2015, for his research on high-efficiency n-i-p thin-film silicon solar cells.

Between 2015 and 2017, he was a Postdoctoral Researcher with the Delft University of Technology, focusing on poly-Si carrier-selective passivating contacts and their application in high-efficiency interdigital back-contacted c-Si solar cells. From January 2018 to June 2018, he was a Postdoctoral Researcher with the Eindhoven University of Technology. Since

July 2018, he has been with the Delft University of Technology, working on carrier-selective passivating contacts based on poly-Si and its alloys, and transition metal-oxides.



Olindo Isabella received the Ph.D. degree (*cum laude*) from the Delft University of Technology, Delft, The Netherlands, in 2013, for his research on light management in thin-film silicon solar cells.

Between 2013 and 2017, he was an Assistant Professor with the Delft University of Technology, and in October 2017, he became an Associate Professor. Since 2019, he has been an appointed Head of the Photovoltaic Materials and Devices Group, where he supervises optoelectrical device modeling activities, novel concepts of light management, development of

high-efficiency solar cells based on crystalline silicon and thin-film silicon technologies, and advanced power modeling for custom photovoltaic systems.



Miro Zeman received the Ph.D. degree (*cum laude*) from the Slovak University of Technology, Bratislava, Slovakia, in 1989, for his research on amorphous silicon.

In 2009, he was appointed as a Full Professor with the Delft University of Technology, Delft, The Netherlands, where he founded the Photovoltaic Materials and Devices Group and currently leads the Electrical Sustainable Energy Department. He is a leading expert in light management, modeling, and the development and application of novel materials

and nanostructures in silicon-based solar systems.